nature physics

Article

https://doi.org/10.1038/s41567-023-02363-2

Demonstration of hot-spot fuel gain exceeding unity in direct-drive inertial confinement fusion implosions

Received: 23 February 2023

Accepted: 29 November 2023

Published online: 05 February 2024

Check for updates

C. A. Williams[1,2] ✉, R. Betti[1,2,3], V. Gopalaswamy[1], J. P. Knauer[1], C. J. Forrest[1], A. Lees[1], R. Ejaz[1,3], P. S. Farmakis[1,3], D. Cao[1], P. B. Radha[1], K. S. Anderson[1], S. P. Regan[1,3], V. Yu Glebov[1], R. C. Shah[1], C. Stoeckl[1], S. Ivancic[1], K. Churnetski[1,3], R. T. Janezic[1], C. Fella[1], M. J. Rosenberg[1], M. J. Bonino[1], D. R. Harding[1], W. T. Shmayda[1], J. Carroll-Nellenback[1,2], S. X. Hu[1], R. Epstein[1], T. J. B. Collins[1], C. A. Thomas[1], I. V. Igumenshchev[1], V. N. Goncharov[1,3], W. Theobald[1,3], K. M. Woo[1], J. A. Marozas[1], K. A. Bauer[1], S. Sampat[1], L. J. Waxer[1], D. Turnbull[1], P. V. Heuer[1], H. McClow[1], L. Ceurvorst[1], W. Scullin[1], D. H. Edgell[1], M. Koch[1], D. Bredesen[1], M. Gatu Johnson[4], J. A. Frenje[4], R. D. Petrasso[4], C. Shuldberg[5], M. Farrell[5], J. Murray[5], D. Guzman[5], B. Serrato[5], S. F. B. Morse[1], M. Labuzeta[1], C. Deeney[1] & E. M. Campbell[1]

Irradiating a small capsule containing deuterium and tritium fuel directly with intense laser light causes it to implode, which creates a plasma hot enough to initiate fusion reactions between the fuel nuclei. Here we report on such laser direct-drive experiments and observe that the fusion reactions produce more energy than the amount of energy in the central so-called hot-spot plasma. This condition is identified as having a hot-spot fuel gain greater than unity. A hot-spot fuel gain of around four was previously accomplished at the National Ignition Facility in indirect-drive inertial confinement fusion experiments where the capsule is irradiated by X-rays. In that case, up to 1.9 MJ of laser energy was used, but in contrast, our experiments on the OMEGA laser system require as little as 28 kJ. As the hot-spot fuel gain is predicted to grow with laser energy and target size, our work establishes the direct-drive approach to inertial fusion as a promising path towards burning and ignited plasmas in the laboratory. Additionally, we report a record (direct-drive) fusion yield of 0.9 kJ on OMEGA, which we achieved with thin-ice deuterium–tritium liner targets.

In laser-driven inertial confinement fusion (ICF)[1–3], energy is rapidly coupled to the surface of a capsule containing cryogenic deuterium–tritium (DT) fuel, which causes its outermost layer to ablate and the remaining spherical shell to implode via momentum conservation (that is, the 'rocket effect'). This energy deposition could come in the form of near-ultraviolet laser light (direct drive)[4], or the soft X-rays of a blackbody radiation field, generated when a high atomic number hohlraum is heated by a laser (indirect drive)[5]. In general, direct-drive

[1]Laboratory for Laser Energetics, University of Rochester, Brighton, NY, USA. [2]Department of Physics and Astronomy, University of Rochester, Rochester, NY, USA. [3]Department of Mechanical Engineering, University of Rochester, Rochester, NY, USA. [4]Plasma Science and Fusion Center, Massachusetts Institute of Technology, Cambridge, MA, USA. [5]General Atomics, San Diego, CA, USA. ✉e-mail: cwilli86@ur.rochester.edu

https://doi.org/10.1038/s41567-023-02363-2

ICF can be viewed as a series of energy transfer steps: laser energy is absorbed via inverse bremsstrahlung in the target's tenuous plasma corona, then carried to the dense fuel payload by electron thermal conduction, and subsequently converted into kinetic energy of the imploding shell. The final transfer process occurs when the kinetic energy of the shell becomes internal energy of the central 'hot-spot' plasma, and the dense DT shell is halted by the hot spot's rising pressure. As the shell reaches stagnation, the hot spot acquires the temperatures and densities required to produce copious thermonuclear fusion reactions D + T → n (14.03 MeV) + α (3.53 MeV).

In general, performance is improved either by designing a more robust implosion, so that the adverse effects of hydrodynamic instabilities[6,7] are lessened, or by enhancing the energy coupled to the capsule. The former method was the primary source of improvement for the Omega Laser Facility at the University of Rochester's Laboratory for Laser Energetics from 2016 to 2018, a period that saw the maximum neutron yield Y_n rise from 5×10^{13} to 1.5×10^{14}. This surge[8] was made possible through the use of statistical models[9,10] that allow individual degradation mechanisms to be identified and addressed. While statistical modelling has been an indispensable tool for limiting yield degradation, yield is not the sole concern of experiments on the OMEGA laser system. The purpose of controlled fusion is to generate the thermonuclear instability known as 'ignition'. In ICF, the onset of ignition occurs when fusion α particles deposit enough energy in the hot spot to outweigh losses due to thermal conduction, radiation and, when the hot spot eventually succeeds in repelling its confining shell, the plasma expansion. Ignition leads to a rapid increase in the hot-spot temperature, thereby driving a burn wave through the cold dense fuel that confines it[11,12]. A metric used to assess the proximity of an implosion to ignition is the Lawson criterion χ (with $\chi\approx1$ corresponding to ignition), derived originally as $\chi\equiv(P\tau)/(P\tau)_{\rm ignition}$, where P is the hot-spot pressure and τ is the confinement time[13]. The Lawson criterion can be recast[14] in terms of the neutron yield Y_{16} (in units of 10^{16} neutrons), the stagnated fuel mass $M_{\rm stag}$ (in mg) and the areal density ρR (in g cm^{-2})

$$\chi=(\rho{\rm R})^{0.61}\left(\frac{0.12Y_{16}}{M_{\rm stag}}\right)^{0.34},\qquad(1)$$

and it is this form of χ that is used to gauge progress in OMEGA implosions. The laser energy available on OMEGA is insufficient to drive a fuel assembly with enough mass and areal density to ignite. OMEGA delivers ~30 kJ of ultraviolet light to tens of micrograms of fuel, while megajoules of driver energy and a fuel mass on the order of miligrams are required for hot-spot ignition (with the target mass scaling linearly with laser energy). However, the Lawson parameter is still relevant for sub-ignition-scale experiments on OMEGA, where it not only is used as a hydrodynamic scaling[15–17] tool (Methods) but also plays a crucial role in navigating the experimental design space from an energetics perspective. Indeed, the fusion energy E_f can be written as the product of χ and the internal energy of the hot spot E_{hs} (see Methods for details) as

$$E_f\propto E_{hs}\chi.\qquad(2)$$

Two main takeaways are readily apparent from equation (2). First, although the main function of the Lawson parameter is to gauge how close an implosion is to igniting, it also serves as a proxy for the hot-spot fuel gain, which we define as the ratio of the fusion energy output to the hot-spot internal energy ($G_{hs}\equiv E_f/E_{hs}$). The constant of proportionality between G_{hs} and χ can be determined from simulations.

Figure 1 displays an ensemble of implosions simulated in the one-dimensional radiation–hydrodynamic code LILAC[18], with $\chi\le0.4$. Each data point corresponds to a post-shot simulation of an OMEGA experiment where the target specifications (size and layer thicknesses) and experimental laser pulse are fed directly into LILAC. For implosions on OMEGA, the hot spot is nearly transparent to the 3.5 MeV α particles born in DT fusion reactions and escape the hot spot without depositing their energy. Because the ion temperature, and hence the yield, is minimally affected by α heating, it has been turned off in the simulations presented in Fig. 1. A linear fit applied to these simulated data reveals

$$G_{hs}=8.83\chi-0.58,$$

which predicts a hot-spot gain of unity when $\chi\approx0.18$. In these simulations, shots begin surpassing $G_{hs}=1$ when χ is as low as 0.15, while every shot satisfies the condition if $\chi>0.2$. The aforementioned improvements made by the statistical modelling approach not only tripled the yield[8] but also pushed χ to the region where G_{hs} on OMEGA would be expected to exceed 1.

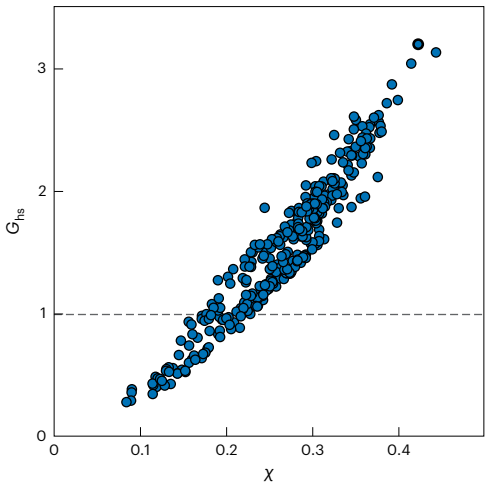

Fig. 1 | The hot-spot fuel gain G_{hs} versus the Lawson parameter χ for a collection of LILAC simulations. We define G_{hs} as the ratio of the fusion energy to the hot-spot internal energy. The threshold $G_{hs}=1$ (dashed line) does not correspond to a unique value of χ but occurs at $\chi=0.18$ for both linear and quadratic fits. On OMEGA, α heating has a negligible effect on yield and hot-spot energy, so χ may be calculated with α energy deposition turned off.

The second important consequence of equation (2) is that further increases in yield (above the mark set in 2018) by factors of two or more on OMEGA necessitate a boost in E_{hs}, specifically. This is because raising χ by similar factors could only realistically be achieved with a change in the experimental scale itself, that is, by using an entirely new driver with a drastic increase in energy.

The National Ignition Facility (NIF) has probed this area of parameter space for nearly a decade. The first experimental demonstration of fusion energy exceeding the energy coupled to the fuel was in indirect-drive experiments fielded on the NIF, reported on in 2014 (ref. 19). The implosions discussed in that work used ~1.9 MJ of laser energy to transfer 3.5–4.4 kJ to the hot spot, ultimately resulting in 14.4–17.3 kJ of fusion energy. These experiments were also noteworthy because they released more fusion energy than the kinetic energy of the in-flight shell. It was also determined that shot N131119 from that study had a yield twice as high as what would have been generated in the absence of α heating, a key milestone on the path to creating laboratory burning plasmas[20] and, eventually, ignition[21,22].

The current work details the earliest experiments to achieve hot-spot gain exceeding unity in cryogenic direct-drive ICF, accomplished on the OMEGA laser with a pulse energy as low as 28 kJ and negligible yield amplification from α heating. Achieving this result with a kilojoule-class laser has important implications for the prospect of pursuing ICF with megajoule-class lasers in a direct-drive format. In the companion paper to this publication, ref. 23 assert that these most recent shots would produce 1.6 ± 0.3 MJ if they were hydrodynamically

https://doi.org/10.1038/s41567-023-02363-2

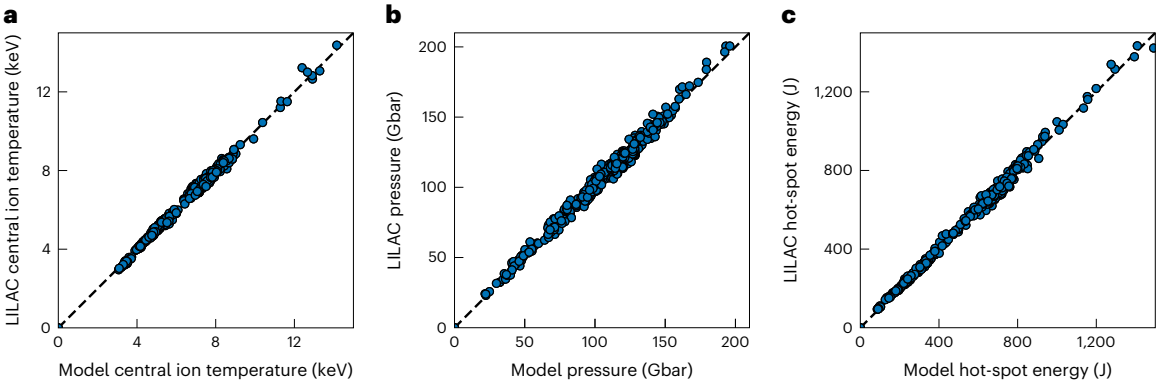

Fig. 2 | Examples of the hot-spot inference model reproducing simulated stagnation metrics. First, OMEGA implosions are simulated in LILAC. **a**–**c**, The hot-spot inference model then uses synthetic data from these simulations to infer bang-time core conditions of the implosions for central ion temperature (**a**), pressure (**b**) and hot-spot energy (**c**). Points along the dashed lines correspond to perfect agreement between the values calculated from the inference model and the values extracted directly from the simulation outputs. Strong agreement is observed among a host of parameters and wide range of values, showing that the model is robust against changes in design.

scaled to use 2.15 MJ of direct-drive laser energy (the capacity of the NIF in indirect drive). In this Article, we first address how the hot-spot energy is determined, before discussing the adjustments that made the $G_{hs} > 1$ feat possible, then summarize the impact of these results. Additionally, we explain the theoretical underpinnings of how the neutron yield was doubled in the latest OMEGA experiments, going from $\sim 1.6 \times 10^{14}$ at the beginning of 2021 to 3.1×10^{14} by the end of that year (which translates to the fusion energy increasing from 0.45 to 0.88 kJ), a record mark in cryogenic direct drive as well as the most fusion energy produced with a sub-megajoule-class laser.

Hot-spot inference model

Naturally, asserting with confidence that the fusion energy has surpassed the internal energy of the hot spot requires both of these values to be calculated in a reliable manner. In the case of the fusion energy, the calculation is relatively straightforward. Each DT fusion reaction produces a single 14 MeV neutron. Determining the fusion energy is therefore tantamount to measuring the neutron yield[24].

Discerning the hot-spot internal energy is less routine. To begin with, there is no one-to-one correlation between the hot-spot energy and a lone observable like there is in the case of fusion energy and neutron yield. Instead, we are left to infer the hot-spot internal energy by finding the spatial profile of the hot-spot pressure and then integrating it throughout the hot-spot volume. Furthermore, the value that is ultimately settled on is influenced by the choice of the theoretical model used for constraint. This work is not the first to infer the energy content of an ICF hot spot[25,26]. The model we have constructed, however, includes several features that are not typically included in such evaluations. The most meaningful additions are: (1) the inclusion of monotonically decreasing pressure profiles instead of isobaric (flat) profiles and (2) allowing the electron and ion temperatures to differ from one another. Momentum conservation leads to spatial variations in pressure when the implosion velocity is a substantial fraction of the hot-spot sound speed, and the electron and ion temperatures differ because their equilibration time is comparable to the burnwidth (~60 ps) in high-performance OMEGA implosions. Including both of these effects is essential if the hot-spot core conditions are to be obtained with the highest degree of accuracy. For the fastest implosions on OMEGA, the pressure at the edge of the hot spot can be as low as 50% of the value at the centre[27], making evident the need for a non-isobaric model. Assuming thermal equilibration on OMEGA would artificially increase the hot-spot pressure by around 15%. Instead of assuming an isobaric hot spot, or describing the radial profiles of the partial pressures and temperatures with analytic functions that are left unaltered across all shot designs, we have opted to take the shape of these profiles from LILAC simulations and to glean their magnitudes from observables acquired using neutron and X-ray diagnostics[24,28–31]. A full description of the model used in this study is provided in Methods, and an example of an experimental X-ray image is provided in Extended Data Fig. 1.

Our model was first tested on synthetic experiments. We applied the model's procedure to the same database of simulated OMEGA experiments that was presented in Fig. 1 and used synthetic neutron and X-ray data from those same simulations to infer properties of the hot spot. The strong agreement between the simulated hot-spot core conditions at bang time (the time of peak neutron production) and those inferred by the model is displayed in Fig. 2. Note that the model accurately recovers the state of the simulated hot spot across a remarkably diverse collection of shots. The outer diameters (ODs) in the set lie in the range of 760–1,060 µm, while the ice thicknesses are as thin as 25 µm and as thick as 85 µm. The laser pulses used across the database are similarly varied. The dissimilar initial conditions lead to hot-spot environments that explore a wide parameter space. The central ion temperatures extend from 3 to 15 keV, while the pressures and energies span an order of magnitude across the database.

Design improvements

Many prior improvements in performance have revolved around stability and symmetry control, using techniques such as intentionally prescribing target offsets to mitigate low-mode asymmetries[32] or moving to smaller target outer diameters to promote better illumination uniformity. The adjustments that followed, however, have focused primarily on one concept: coupling efficiency to the hot spot. Mathematically, the series of direct-drive transfer processes can be represented by the product of the laser energy E_L with three efficiencies η as

$$E_{hs} = E_L \eta_{abs} \eta_{hydro} \eta_{hs}. \quad (3)$$

Here, η_{abs} is the absorption fraction, the hydrodynamic efficiency η_{hydro} is the conversion of absorbed energy to shell kinetic energy (rocket efficiency) and η_{hs} is the transfer of kinetic energy to internal energy of the hot spot. In addition to delivering more energy to the capsule surface (detailed in Methods), a dedicated effort to improve the effectiveness of the incident energy is equally important. The absorption fraction is diminished mainly by cross-beam energy transfer (CBET), which allows the light of incoming edge rays to be redirected into outgoing rays that are refracted away from the target[33]. One way to combat this is by imploding larger-OD capsules so more rays are normally

https://doi.org/10.1038/s41567-023-02363-2

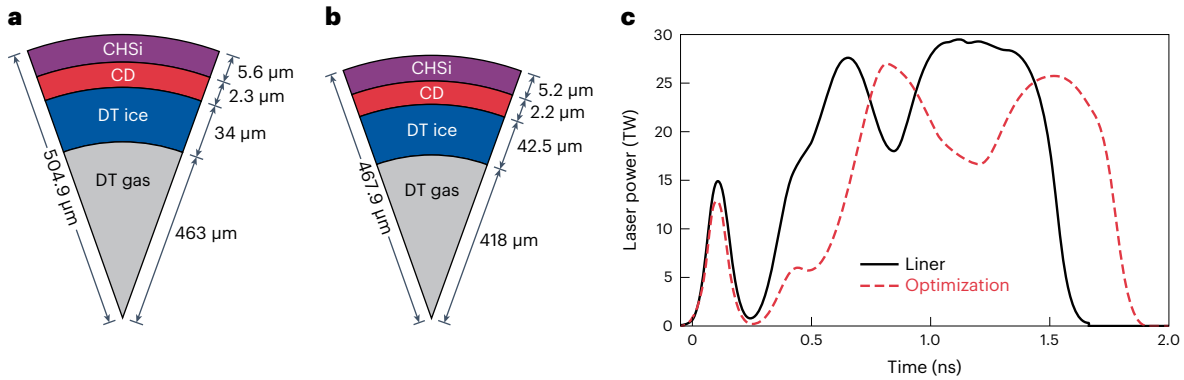

Fig. 3 | Target and laser pulse comparisons between the thin-ice DT liner campaign and χ-optimization campaign. a, An example thin-ice DT liner target optimized to produce the highest possible fusion yield. **b**, In contrast, a target intended to optimize the Lawson criterion χ. The liner in **a** has a much higher surface area and thinner ice layer than the χ-optimization target, which leads to an implosion with ultra-high velocity (~600 km s^{-1}), in contrast to the level of ~500 km s^{-1} accessed in χ-optimization shots. Both targets have bi-layer plastic ablators: the hydrocarbon (CH) outer layer doped with silicon (CHSi) promotes better laser absorption and laser–plasma instability mitigation, while the deuterated hydrocarbon (CD) layer beneath maintains the hydrodynamic efficiency. **c**, A comparison of the 30.8 kJ multi-pulse driver laser pulse of a DT liner versus the 28.5 kJ SSD pulse of a χ-optimization shot.

incident on the target and less refract. However, this can have a negative effect on stability because it leads to higher in-flight aspect ratios (IFAR, calculated as shell radius/shell thickness) and lower beam-to-target radius ratios (R_b/R_t). Both of these jeopardize the shell integrity and make it susceptible to ρR degradation and in-flight break-up[34]. Instead of increasing the outer diameter indefinitely, mid-Z dopants can be added to the ablator to foster greater collisional absorption of the incoming 'pump' rays and higher coronal temperatures, both of which reduce the CBET[33]. Laser energy is transferred to the plasma by causing collisions between ions in the corona against electrons oscillating in the electric field of the laser light. The presence of a dopant such as silicon ($Z = 14$), for example, facilitates a faster rate of collisions[3,35]. Adding as little as 5–7% (by atomic fraction) of silicon has been shown to enhance the absolute absorption on OMEGA by 10% through 'A/B' comparisons where the same laser pulse is used on targets with/without silicon. The inclusion of silicon serves the added benefit of diminishing the production of suprathermal electrons arising from the two-plasmon-decay instability[35,36], which prematurely heat the in-flight shell and cause it to decompress[37,38], leading to lower ρR and lower χ. Thus, silicon addresses various sources of degradation that limit G_{hs} while simultaneously raising the hot-spot and fusion energies above the implosions reported on by ref. 8 in 2019 that used similar pulses on glow-discharge polymer (GDP) ablators (referred to below as GDP 'χ-optimization').

Although generating more yield is an important factor in increasing χ, the designs that optimize χ do not necessarily optimize yield simultaneously. The latter consideration requires an approach that is more focused on one-dimensional (1D) characteristics. In essence, this means optimizing the yield by augmenting coupling to the hot spot, even at the cost of slightly reducing χ. The thin-ice DT liner is a class of target devised by ref. 27 explicitly for this purpose. These targets are intended to maximize energy absorption by putting as much as possible onto the largest-OD targets available. Figure 3 compares a DT liner target with one meant to optimize the Lawson criterion. Because the payload velocity diverges logarithmically with remaining mass fraction (in the simple rocket model[3]), starting off with a thin ice layer boosts η_{hydro} and enables implosion velocities as high as 600 km s^{-1}. Because the mass ablation rate of indirect drive is roughly ten-fold higher than in direct drive, the hydrodynamic efficiency of laser-driven shells cannot compete with X-ray drive. Yet, direct-drive implosions make up for this gap by circumventing additional loss mechanisms that are present in indirect drive, such as finite hohlraum albedo. Additionally, an indirect-drive target sits in a radiation bath that is isotropic and therefore never encounters many of the X-rays present in the cavity. In totality, out of the 2 MJ initially incident on a NIF hohlraum, approximately 15–20 kJ ends up as fuel kinetic energy[39] (close to 30 kJ if the diamond ablator kinetic energy is added). The absorption in direct drive on OMEGA helps the shell acquire 1.5–2 kJ of kinetic energy and is therefore ~5× more efficient at turning laser energy into kinetic energy.

One of the key components to realizing ignition on the NIF was improving the conversion of kinetic energy to internal energy by decreasing coast time, to avoid early decompression of the shell[40]. This is because a thin, dense shell stagnates all at once like a hard piston, in contrast to a distended, puffy shell that struggles to do work on the hot spot[41]. The functional dependencies of the simulated transfer efficiency from shell-kinetic to hot-spot internal energy can be obtained from a non-linear regression on the IFAR and the adiabat α. This is shown in Fig. 4a, where α is defined as the ratio of pressure in the shell to the Fermi-degenerate pressure of a fully ionized DT plasma at the shell density. The fit leads to the relation

$$\eta_{hs} = (0.0456)\mathrm{IFAR}^{0.85}\alpha^{0.22}. \quad (4)$$

This trend is corroborated in experiment, as illustrated by Fig. 4b, which shows that high-IFAR, ultra-high-velocity liners are capable of delivering the most energy to the hot spot. The transfer efficiency is reduced by roughly 15% in experiment with respect to the 1D simulations. Three-dimensional effects such as low-mode asymmetries allow the shell to retain kinetic energy even at peak compression, which ultimately degrades the hot-spot pressure and yield[42].

Table 1 provides a summary of experimental results from a selection of OMEGA implosions. Upon inspection, the table supports a number of expected trends. First, while the large IFAR values of liners give rise to their elevated transfer efficiencies, the only way to stave off the instabilities that would otherwise break the shell apart is to raise their adiabat (entropy)[27,43–47]. This comes at the detriment of target convergence, which keeps their hot-spot pressure low. The liners are able to produce high yields in spite of these low pressures, not just because of the high temperature at the core but also because it remains above thermonuclear temperatures (~1 keV) out to a considerable radius. In other words, what liners lack in terms of density, they make up for with sheer volume. For instance, the hot-spot volume of shot number 102360 is ~3.5 fold larger than that of shot number 102154, and it produces more yield despite having less than half the hot-spot pressure. This realization gives added understanding to the high transfer efficiencies of liners displayed in Fig. 4. The extra energy coupled to the hot spot in liner implosions does not manifest as elevated energy

https://doi.org/10.1038/s41567-023-02363-2

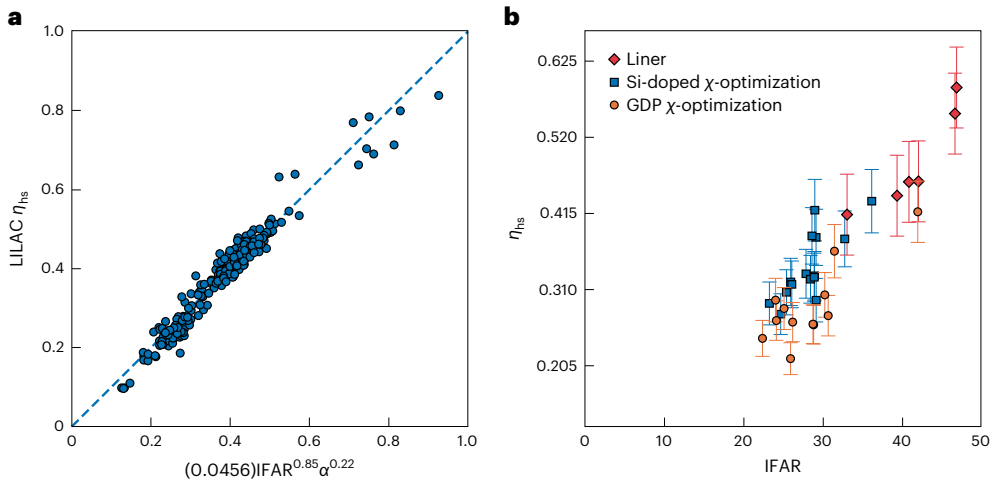

Fig. 4 | The transfer efficiency η_{hs} of kinetic to internal energy in both simulation and experiment. a, A predictive model for the transfer efficiency from shell kinetic energy to hot-spot internal energy in 1D simulations. The dashed line represents a perfect prediction. The only variables used to train this model are the IFAR and adiabat α, which finds $\eta_{hs} = (0.0456)\mathrm{IFAR}^{0.85}\alpha^{0.22}$, although a similar model can be formed that finds $\eta_{hs} \propto v_{imp}^{1.9}$. **b**, Experimental values of the transfer efficiency from shell kinetic energy to hot-spot internal energy in OMEGA direct-drive implosions. Error bars represent one standard deviation. The plot verifies that the IFAR is the dominant force in determining transfer efficiency. The high-IFAR DT liner implosions[27] (red diamonds) demonstrate higher efficiency than χ-optimization implosions using either GDP ablators[8,48] (orange dots) or silicon-doped hydrocarbon (CHSi) plastic (blue squares). In experiment, unlike 1D simulations, low-mode perturbations also have an effect on transfer efficiency, as residual kinetic energy impedes efficient conversion to internal energy, which is responsible for the reduction in η_{hs}.

Table 1 | Experimental results of three high-performance OMEGA implosions

Shot number	OD/Δ_{DT} (μm)	E_f/E_{hs} (J)	χ	α	V_{hs} (10^5 μm^3)	$\langle T_i\rangle/T_0$ (keV)[a]	$\langle P\rangle/P_0$ (Gbar)
102154	935.3/44.5	627/603	0.19	5.1	0.61	4.7/6.6	73.6/76.3
102360[b,c]	1,013.4/34.6	747/812	0.13	8.9	2.11	6.0/8.4	32.0/34.9
103952[c]	1,018.0/39.5	871/838	0.16	6.3	1.50	5.8/8.2	43.2/46.2

The capsule outer diameter and initial ice thickness are labelled as OD and Δ_{DT}, respectively. The fusion energy E_f is the total energy released in both the neutrons and α particles. The hot-spot energy E_{hs}, Lawson criterion χ, total central pressure (ion plus electron) P_0 and central ion temperature T_0 are determined by using the hot-spot inference model devised for this study. $\langle T_i\rangle$ and $\langle P\rangle$ are the neutron-averaged ion temperature and neutron-averaged total pressure, respectively. The adiabat α is the ratio of the plasma pressure to the Fermi-degeneracy pressure during the acceleration phase. The hot-spot volume V_{hs} is obtained using X-ray images as explained in Methods. [a]The minimum ion temperature measured among a suite of neutron time-of-flight (nTOF) detectors located along various lines of sight. [b]The only capsule without Si dopant. [c]Thin-ice DT liner.

density (pressure) but rather by heating up a larger volume of plasma in accordance with the predictions presented in ref. 27. Additionally, note that shot number 102360 falls below the χ range (0.15–0.2 according to Fig. 1) where G_{hs} is expected to surpass unity, which is validated experimentally. By contrast, shots number 102154 and 103952 have Lawson parameters that reside within this range and indeed produce $G_{hs} > 1$.

When the hot-spot inference model is applied to the experimental database of past shots on OMEGA, it is revealed that a number of recent implosions, including a number of thin-ice DT liners, demonstrate fusion outputs larger than the internal energy of the hot spot required to induce the fusion reactions therein. Recall that, on OMEGA, heating of the hot spot comes almost exclusively from the piston-like compression performed by the surrounding dense shell. The dimensions of the hot spot are smaller than the mean free path of the 3.5 MeV α particles created in DT fusion reactions[3], and therefore the level of α heating generated in these implosions has a negligible effect on both the yield and internal energy. The importance of creating yield on the strength of compression alone is that this is a key ingredient even in ignition-scale implosions, because ignition is a dynamical process. If a hot spot is unable to produce a high reaction rate during the compression phase of the implosion, α deposition will be inconsequential even if the assembly is much larger than the α mean free path, since the energy carried by the fusion products will be negligible with respect to the hot-spot energy (which is why χ has an explicit yield dependence in equation (1) in addition to ρR). In every DT reaction, 20% of the energy release is imparted to the α particle, meaning $E_\alpha > 0.2E_{hs}$ when $G_{hs} > 1$.

As a consequence of equation (2), the slope of an E_f versus E_{hs} plot represents a measure of implosion quality and is proportional to χ. Figure 5 shows the fusion energy plotted against the hot-spot energy for a series of recent OMEGA implosions, with a slight majority corresponding to $G_{hs} > 1$. That this demonstration was realized with only ~30 kJ is noteworthy because of the potential benefits that may lie in hydrodynamically scaled versions of these shots. While E_{hs} scales linearly with laser energy, the fusion energy scales faster, even in the absence of α heating. In 1D, $E_f \propto E_L^{1.43}$, primarily because the confinement time scales with target radius, but also because the temperature improves with size as a result of weaker thermal conduction losses. In spherical geometry, the ratio of surface area to volume grows with radius R like $1/R$, so the heat flux from the hot spot to the cold shell has a smaller impact for large targets. When the α particle energy deposition becomes an important factor at ignition-relevant scales, it too has a more pronounced effect on the fusion energy than it does on internal energy. This is because the energy of the hot spot is proportional to its temperature T, while the temperature dependence of the fusion reactivity $\langle\sigma v\rangle$ is much stronger ($\langle\sigma v\rangle \propto T^4$ at a few kiloelectron volts)[3]. Even below the ignition threshold, it is possible for the main contribution to the hot-spot energy to come from α particle deposition, eclipsing the compression work done by the shell. This distinction, referred to as the burning plasma regime, is inaccessible on OMEGA owing to the aforementioned energy deficit. However, ref. 23 report that the highest performing implosions on OMEGA have entered a regime where, if hydroscaled to 2.15 MJ of laser drive, would indeed produce a burning plasma.

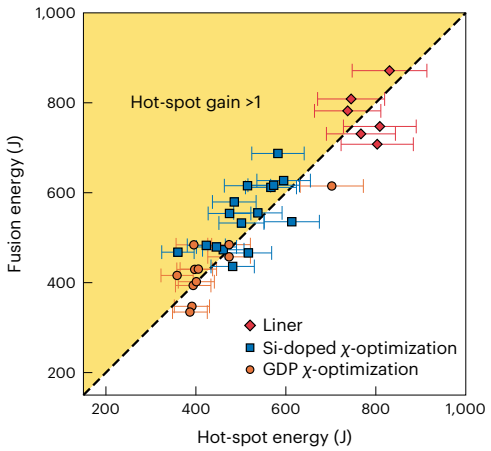

Fig. 5 | Fusion energy versus hot-spot energy in recent implosions on OMEGA. The figure shows hot-spot gain above unity (yellow shading) being achieved in campaigns intended to optimize χ with GDP capsules[8,48], silicon-doped targets from the optimization campaign and thin-ice DT liner targets[27] intended to boost yield. Error bars represent one standard deviation.

Online content

Any methods, additional references, Nature Portfolio reporting summaries, source data, extended data, supplementary information, acknowledgements, peer review information; details of author contributions and competing interests; and statements of data and code availability are available at https://doi.org/10.1038/s41567-023-02363-2.

References

1. Nuckolls, J., Wood, L., Thiessen, A. & Zimmerman, G. Laser compression of matter to super-high densities: thermonuclear (CTR) applications. *Nature* **239**, 139–142 (1972).
2. Betti, R. & Hurricane, O. Inertial-confinement fusion with lasers. *Nat. Phys.* **12**, 435–448 (2016).
3. Atzeni, S. & Meyer-Ter-Vehn, J. *The Physics of Inertial Fusion: Beam Plasma Interaction, Hydrodynamics, Hot Dense Matter* (Clarendon Press, 2004).
4. Craxton, R. S. et al. Direct-drive inertial confinement fusion: a review. *Phys. Plasmas* **22**, 110501 (2015).
5. Lindl, J. Development of the indirect-drive approach to inertial confinement fusion and the target physics basis for ignition and gain. *Phys. Plasmas* **2**, 3933–4024 (1995).
6. Rayleigh, J. W. S. B. *Scientific Papers: 1881–1887*, vol. 2 (Univ. Press, 1900).
7. Brouillette, M. The Richtmyer–Meshkov instability. *Annu. Rev. Fluid Mech.* **34**, 445–468 (2002).
8. Gopalaswamy, V. et al. Tripled yield in direct-drive laser fusion through statistical modelling. *Nature* **565**, 581–586 (2019).
9. Lees, A. et al. Experimentally inferred fusion yield dependencies of OMEGA inertial confinement fusion implosions. *Phys. Rev. Lett.* **127**, 105001 (2021).
10. Lees, A. et al. Understanding the fusion yield dependencies in OMEGA DT-layered implosion experiments using a physics-based statistical mapping model. *Phys. Plasmas* **30**, 012709 (2023).
11. Christopherson, A. R. et al. A comprehensive alpha-heating model for inertial confinement fusion. *Phys. Plasmas* **25**, 012703 (2018).
12. Christopherson, A., Betti, R. & Lindl, J. Thermonuclear ignition and the onset of propagating burn in inertial fusion implosions. *Phys. Rev. E* **99**, 021201 (2019).
13. Lawson, J. D. Some criteria for a power producing thermonuclear reactor. *Proc. Phys. Soc. B* **70**, 6–10 (1957).
14. Betti, R. et al. Thermonuclear ignition in inertial confinement fusion and comparison with magnetic confinement. *Phys. Plasmas* **17**, 058102 (2010).
15. Zhou, C. & Betti, R. A measurable Lawson criterion and hydro-equivalent curves for inertial confinement fusion. *Phys. Plasmas* **15**, 102707 (2008).
16. Bose, A., Woo, K., Nora, R. & Betti, R. Hydrodynamic scaling of the deceleration-phase Rayleigh–Taylor instability. *Phys. Plasmas* **22**, 072702 (2015).
17. Goncharov, V. N. et al. Improving the hot-spot pressure and demonstrating ignition hydrodynamic equivalence in cryogenic deuterium–tritium implosions on OMEGA. *Phys. Plasmas* **21**, 056315 (2014).
18. Delettrez, J., Epstein, R., Richardson, M. C., Jaanimagi, P. A. & Henke, B. L. Effect of laser illumination nonuniformity on the analysis of time-resolved x-ray measurements in UV spherical transport experiments. *Phys. Rev. A* **36**, 3926–3934 (1987).
19. Hurricane, O. et al. Fuel gain exceeding unity in an inertially confined fusion implosion. *Nature* **506**, 343–348 (2014).
20. Zylstra, A. et al. Burning plasma achieved in inertial fusion. *Nature* **601**, 542–548 (2022).
21. Kritcher, A. L. et al. Design of an inertial fusion experiment exceeding the Lawson criterion for ignition. *Phys. Rev. E* **106**, 025201 (2022).
22. Zylstra, A. B. et al. Experimental achievement and signatures of ignition at the National Ignition Facility. *Phys. Rev. E* **106**, 025202 (2022).
23. Gopalaswamy, V. et al. Demonstration of a hydrodynamically equivalent burning plasma in direct-drive inertial confinement fusion. *Nature Physics*. https://doi.org/10.1038/s41567-023-02361-4 (2024).
24. Frenje, J. A. Nuclear diagnostics for inertial confinement fusion (ICF) plasmas. *Plasma Phys. Control. Fusion* **62**, 023001 (2020).
25. Cerjan, C., Springer, P. T. & Sepke, S. M. Integrated diagnostic analysis of inertial confinement fusion capsule performance. *Phys. Plasmas* **20**, 056319 (2013).
26. Zylstra, A. B., Nora, R., Patel, P. & Hurricane, O. Model validation for inferred hot-spot conditions in National Ignition Facility experiments. *Phys. Plasmas* **28**, 122703 (2021).
27. Williams, C. A., Betti, R., Gopalaswamy, V. & Lees, A. High yields in direct-drive inertial confinement fusion using thin-ice DT liner targets. *Phys. Plasmas* **28**, 122708 (2021).
28. Stoeckl, C. et al. Neutron temporal diagnostic for high-yield deuterium–tritium cryogenic implosions on OMEGA. *Rev. Sci. Instrum.* **87**, 053501 (2016).
29. Theobald, W. et al. The single-line-of-sight, time-resolved x-ray imager diagnostic on OMEGA. *Rev. Sci. Instrum.* **89**, 10G117 (2018).
30. Moore, A. S. et al. Neutron time of flight (nToF) detectors for inertial fusion experiments. *Rev. Sci. Instrum.* **94**, 061102 (2023).
31. Churnetski, K. et al. Three-dimensional hot-spot x-ray emission tomography from cryogenic deuterium–tritium direct-drive implosions on OMEGA. *Rev. Sci. Instrum.* **93**, 093530 (2022).
32. Mannion, O. M. et al. Mitigation of mode-one asymmetry in laser-direct-drive inertial confinement fusion implosions. *Phys. Plasmas* **28**, 042701 (2021).
33. Igumenshchev, I. V. et al. Crossed-beam energy transfer in implosion experiments on OMEGA. *Phys. Plasmas* **17**, 122708 (2010).
34. Baltazar, J. et al. Diagnosing low-mode ($l<6$) and mid-mode ($6\leq l\leq 60$) asymmetries in the post-stagnation phase of laser-direct-drive deuterium–tritium cryogenic implosions on OMEGA. *Rev. Sci. Instrum.* **93**, 123513 (2022).
35. Kruer, W. *The Physics of Laser Plasma Interactions* (CRC Press, 2019).
36. Seka, W. et al. Two-plasmon-decay instability in direct-drive inertial confinement fusion experiments. *Phys. Plasmas* **16**, 052701 (2009).

37. Christopherson, A. et al. Direct measurements of DT fuel preheat from hot electrons in direct-drive inertial confinement fusion. *Phys. Rev. Lett.* **127**, 055001 (2021).
38. Christopherson, A. et al. Inferences of hot electron preheat and its spatial distribution in OMEGA direct drive implosions. *Phys. Plasmas* **29**, 122703 (2022).
39. Zylstra, A. et al. Record energetics for an inertial fusion implosion at NIF. *Phys. Rev. Lett.* **126**, 025001 (2021).
40. Hurricane, O. A. et al. Beyond alpha-heating: driving inertially confined fusion implosions toward a burning-plasma state on the National Ignition Facility. *Plasma Phys. Control. Fusion* **61**, 014033 (2018).
41. Betti, R. et al. Deceleration phase of inertial confinement fusion implosions. *Phys. Plasmas* **9**, 2277–2286 (2002).
42. Woo, K. M. et al. Effects of residual kinetic energy on yield degradation and ion temperature asymmetries in inertial confinement fusion implosions. *Phys. Plasmas* **25**, 052704 (2018).
43. Anderson, K. & Betti, R. Theory of laser-induced adiabat shaping in inertial fusion implosions: the decaying shock. *Phys. Plasmas* **10**, 4448–4462 (2003).
44. Goncharov, V. N. et al. Improved performance of direct-drive inertial confinement fusion target designs with adiabat shaping using an intensity picket. *Phys. Plasmas* **10**, 1906–1918 (2003).
45. Anderson, K. & Betti, R. Laser-induced adiabat shaping by relaxation in inertial fusion implosions. *Phys. Plasmas* **11**, 5–8 (2004).
46. Knauer, J. P. et al. Improved target stability using picket pulses to increase and shape the ablator adiabat. *Phys. Plasmas* **12**, 056306 (2005).
47. Betti, R. et al. Theory of laser-induced adiabat shaping in inertial fusion implosions: the relaxation method. *Phys. Plasmas* **12**, 042703 (2005).
48. Regan, S. P. et al. Demonstration of fuel hot-spot pressure in excess of 50 Gbar for direct-drive, layered deuterium-tritium implosions on OMEGA. *Phys. Rev. Lett.* **117**, 025001 (2016).

Methods

Relationship between hot-spot fuel gain and the Lawson parameter

The fusion energy is given by

$$E_{\mathrm{f}} = \epsilon_{\mathrm{f}} \int \mathrm{d}t \int \mathrm{d}^3 r\, n_{\mathrm{D}} n_{\mathrm{T}} \langle \sigma v \rangle, \tag{5}$$

where $\varepsilon_{\mathrm{f}} = 17.6$ MeV is the energy released in one DT reaction, n_{D} and n_{T} are the deuteron and triton number densities, respectively, and $<\sigma v>$ is the DT reactivity. Unlike the dense confining shell, it is assumed that the hot-spot plasma is at a sufficiently high temperature and low enough density so as to be neither strongly coupled nor degenerate[3], which permits an ideal gas treatment for the hot-spot equation of state. Under this assumption, $E_{\mathrm{f}} \approx \varepsilon_{\mathrm{f}}(P^2/T^2)<\sigma v>V_{\mathrm{hs}}\tau$, where P and T are the plasma pressure and temperature, respectively, V_{hs} the hot-spot volume and τ is the burnwidth (duration). Manipulating this relation leads to

$$E_{\mathrm{f}} \propto E_{\mathrm{hs}} \left(\frac{P\tau}{T^2/\epsilon_{\mathrm{f}}\langle \sigma v \rangle} \right), \tag{6}$$

where E_{hs} is the internal energy of the hot spot. Recalling that $\chi \equiv (P\tau)/(P\tau)_{\mathrm{ignition}}$ allows for a more transparent representation of the fusion yield to be arranged as

$$E_{\mathrm{f}} \propto E_{\mathrm{hs}} \chi. \tag{7}$$

Defining the hot-spot fuel gain as $G_{\mathrm{hs}} \equiv E_{\mathrm{f}}/E_{\mathrm{hs}}$ leads directly to

$$G_{\mathrm{hs}} = C\chi, \tag{8}$$

where the constant of proportionality C is best determined from radiation–hydrodynamic simulations.

Inferring the hot-spot energy

A direct measurement of the hot-spot internal energy in an ICF implosion is not feasible. However, this quantity can be inferred if neutron and X-ray diagnostics are able to provide the necessary measurements to derive the hot-spot pressure from the neutron yield, ion temperature and hot-spot volume. The latter is inferred from X-ray self-emission images.

The first measurable quantity of interest is the neutron yield Y_{n}. For thermonuclear plasmas, the specific reaction rate (reactions per unit volume, per unit time) R_{ij} between two species i and j is given by

$$R_{ij} = \frac{n_i n_j}{1+\delta_{ij}} \langle \sigma v \rangle_{ij}, \tag{9}$$

where n_i is the number density of species i, $<\sigma v>$ is the reactivity of the reaction in question and δ_{ij} is the Kronecker delta. The total neutron yield from reactions between deuterium and tritium is obtained by integrating the specific reaction rate over time and space as

$$Y_{\mathrm{n}} = \int \mathrm{d}t \int \mathrm{d}^3 r\, n_{\mathrm{D}} n_{\mathrm{T}} \langle \sigma v \rangle, \tag{10}$$

where the subscript has been dropped from the reactivity for brevity. Because the hot-spot plasma has a Coulomb coupling parameter $\Gamma \ll 1$ and is non-degenerate ($T_{\mathrm{i}} \gg T_{\mathrm{F}}$), we are able to use an ideal gas equation of state to relate the ion number density $\mathrm{n_i}$ to the ion partial pressure P_{i} and ion temperature T_{i} as $n_{\mathrm{i}} = P_{\mathrm{i}}/(k_{\mathrm{B}} T_{\mathrm{i}})$. We assume a single temperature for both ion species owing to their relatively small mass difference, but allow for the composition of the plasma to differ from that of an equimolar mixture. The ion number density can then be substituted into the yield equation to yield

$$Y_{\mathrm{n}} = \frac{f_{\mathrm{D}} f_{\mathrm{T}}}{k_{\mathrm{B}}^{\,2}} \int \mathrm{d}t \int \mathrm{d}^3 r \frac{P_{\mathrm{i}}^{\,2}}{T_{\mathrm{i}}^{\,2}} \langle \sigma v \rangle, \tag{11}$$

where f_i is the species fraction of species i and k_{B} is Boltzmann's constant.

Equation (11) can be simplified by substituting static profiles for time-dependent variables and replacing the integral over time with a finite burn duration factor. If the neutron production rate $\dot{Y}$ were a perfectly Gaussian function in time, replacing the temporal integral in equation (11) with the the burnwidth τ (full-width at half-maximum, FWHM) would result in static profiles corresponding to a production rate $\dot{Y}_*$ that is larger than the bang-time rate $\dot{Y}_{\mathrm{bt}}$ by a factor $\sqrt{\pi/\ln(16)} \approx (1.06)$. By definition, the highest neutron rate occurs at the bang time. Therefore, the static profiles need to be depressed. This is handled by replacing the temporal integral with $\tau' = c\tau$, where the constant $c \approx 1.1$ has been determined by imposing $c \equiv Y_{\mathrm{n}}/(\tau \dot{Y}_{\mathrm{bt}})$ and examining an ensemble of 1D simulations. This accounts for the aforementioned 6% increase, along with an additional correction for deviations from Gaussian shape in the neutron signal.

We assume the pressure and temperature to be isotropic, and reconstruct the spatial dependence of these quantities Q by representing them as a dimensionless 'shape function' $\hat{Q}(r)$, multiplied by a central value Q_0 possessing the dimension of Q,

$$Q(r,\theta,\phi) \approx Q_0 \hat{Q}(r),$$

$$\hat{Q}(r=0) = 1.$$

If we also normalize the radial coordinate with the hot-spot radius as $x \equiv r/R_{\mathrm{hs}}$, then the recovered function $\hat{Q}(x)$ can be taken directly from LILAC simulations. That is, we assume that, while the magnitude of the pressure, temperature etc. differ between experiment and simulation, their shapes should be similar.

Using this new formulation, the yield can be rewritten as

$$Y_{\mathrm{n}} = b\tau' \left(\frac{P_{0,\mathrm{i}}^{\,2}}{T_{0,\mathrm{i}}^{\,2}} \right) R_{\mathrm{hs}}^3 \int_0^1 x^2 \frac{\hat{P}_{\mathrm{i}}^{\,2}}{\hat{T}_{\mathrm{i}}^{\,2}} \langle \sigma v \rangle \,\mathrm{d}x, \tag{12}$$

where $b = \left(4\pi f_{\mathrm{D}} f_{\mathrm{T}}/k_{\mathrm{B}}^{\,2}\right)$. Typically the ice layer of an OMEGA target has a D-to-T ratio of 40:60, while the vapour is 50:50. To settle on a single number for each species fraction, LILAC simulations are used to estimate the percentage of yield coming from the vapour and ice, respectively. The appropriate weighting factors are then used to converge on the hot-spot composition. The radial integral in equation (12) is taken from the target origin to the hot-spot boundary. Because the transition from the hot spot to the cold shell is continuous, the value input as the hot-spot edge must be chosen with care. Ideally, this would be acquired via neutron imaging. Although the Omega Laser Facility does not currently have neutron imaging, X-rays can be used instead to find the desired volume. Historically, this is given by the X-ray R_{17} value, that is, the radius at which the X-ray self-emission intensity has decreased to 17% of the maximum intensity. Previous work by ref. 49 shows that photons with energies between 15 and 20 keV are emitted from the same region that produces DT neutrons. Each channel of the spatially resolved electron temperature (SRTe) diagnostic is sensitive to a different photon energy range. The strongest correlation between the R_{17} and the neutron-producing region for shots with temperatures ~5 keV is observed from synthetic data of the SRTe's fourth channel, which detects X-rays with $E_\gamma \approx 20$ keV. These synthetic data show that, in simulations, the region enclosed by the R_{17} from SRTe channel 4 accounts for the vast majority of the neutron source, ranging between 93% and 95% in high-velocity implosions. The X-ray R_{17} is valid even in the presence of ellipticity in the hot-spot shape, as it is obtained from a

two-dimensional super-Gaussian fit. However, it should be noted that the majority of recent high-performing implosions are round and exhibit negligible ellipticity. An experimental SRTe image of shot 102154 is given in Extended Data Fig. 1, having a semi-major axis to semi-minor axis ratio of $a/b = 1.03 \pm 0.02$.

From the neutron time-of-flight (nTOF) spectrum, a burn-averaged ion temperature can be extracted with the form

$$\langle T_i \rangle = \frac{\int dt \int d^3x\, T_i n_D n_T \langle \sigma v \rangle}{\int dt \int d^3x\, n_D n_T \langle \sigma v \rangle}. \tag{13}$$

Applying each of the previous approximations leads to a central ion temperature given by

$$T_{0,i} = \langle T_i \rangle \frac{\int_0^1 x^2 \left(\hat{P}_i/\hat{T}_i\right)^2 \langle \sigma v \rangle \, dx}{\int_0^1 x^2 \left(\hat{P}_i^{\,2}/\hat{T}_i\right) \langle \sigma v \rangle \, dx}. \tag{14}$$

Now that an expression for the central ion temperature has been found, the yield equation can be inverted to isolate the central pressure as

$$P_{0,i} = b^{-1/2} \langle T_i \rangle R_{17}^{-3/2} \sqrt{\frac{Y_n}{\tau'}} \frac{\sqrt{\int_0^1 x^2 \left(\hat{P}_i/\hat{T}_i\right)^2 \langle \sigma v \rangle \, dx}}{\int_0^1 x^2 \left(\hat{P}_i^{\,2}/\hat{T}_i\right) \langle \sigma v \rangle \, dx}. \tag{15}$$

The contribution to the hot-spot internal energy coming specifically from the ions is then simply given by integrating the ion pressure over the volume of the hot spot. The result is

$$E_{hs}^{ion} = \frac{3}{2}(4\pi R_{17}^3) P_{0,i} \int_0^1 x^2 \hat{P}_i dx. \tag{16}$$

The rebound shock and subsequent compression of the hot spot preferentially heat the ions over the electrons. Since the equilibration time between ions and electrons is longer than the burnwidth, the electron temperature is below the ion temperature throughout the hot spot (in the cold shell, the temperatures are similar owing to the faster equilibration time). In a characteristic hot-spot plasma, the Debye length is much shorter than the temperature and density gradient scale lengths. We therefore have the freedom to impose quasi-neutrality $n_i(r) = n_e(r)$ where n_e is the electron number density. This means that the ratio of species pressures at any location is equal to the ratio of temperatures at that same point, including the centre value. We define this central temperature ratio T_{rat} as $T_{rat} \equiv T_e(0)/T_i(0) = P_e(0)/P_i(0)$, where T_e and P_e are the electron temperature and electron pressure, respectively. If we can calculate T_{rat} we will be able to immediately determine the electronic contribution to the hot-spot internal energy.

From the ideal gas equation of state,

$$T_e(r) = P_e(r)\frac{T_i(r)}{P_i(r)} = P_{0,i}\frac{T_{0,e}}{T_{0,i}}\hat{P}_e T_{0,i}\frac{\hat{T}_i}{P_{0,i}\hat{P}_i},$$

or, in terms of our desired variable T_{rat},

$$T_e(r) = T_{0,i} T_{rat} \hat{T}_i \frac{\hat{P}_e}{\hat{P}_i}. \tag{17}$$

It is most useful to connect the central temperature ratio to another experimental observable so as to add one more constraint to our system. In the same fashion as equation (13) defines the neutron-averaged ion temperature, a neutron-averaged electron temperature appears as

$$\langle T_e \rangle = \frac{\int dt \int d^3r\, T_e n_D n_T \langle \sigma v \rangle}{\int dt \int d^3r\, n_D n_T \langle \sigma v \rangle}. \tag{18}$$

Eliminating the electron temperature with equation (17) and applying the same general assumptions and change of variables as before leads to

$$\langle T_e \rangle = T_{0,i} T_{rat} \frac{\int_0^1 x^2 \hat{P}_e \left(\hat{P}_i/\hat{T}_i\right) \langle \sigma v \rangle \, dx}{\int_0^1 x^2 \left(\hat{P}_i/\hat{T}_i\right)^2 \langle \sigma v \rangle \, dx}. \tag{19}$$

It is now beneficial to use equations (19) and (14) to rewrite the temperature ratio in terms of the measured quantities and integrals of known radial profiles. Utilizing equation (15), we obtain the total hot-spot internal energy (represented here in its full, explicit form) as

$$E^{hs} = k_B \langle T_i \rangle R_{17}^{3/2} \sqrt{\frac{9\pi Y_n}{f_D f_T \tau'}} \sqrt{\frac{\int_0^1 x^2 \left(\hat{P}_i/\hat{T}_i\right)^2 \langle \sigma v \rangle \, dx}{\int_0^1 x^2 \left(\hat{P}_i^{\,2}/\hat{T}_i\right) \langle \sigma v \rangle \, dx}} \left[\int_0^1 x^2 \hat{P}_i \, dx + \frac{\langle T_e \rangle}{\langle T_i \rangle} \frac{\int_0^1 x^2 \left(\hat{P}_i^{\,2}/\hat{T}_i\right) \langle \sigma v \rangle \, dx}{\int_0^1 x^2 \hat{P}_e \left(\hat{P}_i/\hat{T}_i\right) \langle \sigma v \rangle \, dx} \int_0^1 x^2 \hat{P}_e \, dx \right]. \tag{20}$$

While the model presented here has been constructed primarily to calculate the hot-spot energy, the information that must be gathered to make that determination can be used to infer other quantities as well. These include scalar quantities such as the hot-spot mass, as well as radial profiles such as the specific reaction rate (equation (9)), or the reaction rate linear density $4\pi n_D n_T \langle \sigma v \rangle r^2$. Uncertainties in the model-estimated parameters are obtained by Monte Carlo sampling, assuming that the uncertainties on the experimental inputs are normally distributed.

Hydrodynamic scaling

For sub-ignition-scale experiments, theory and computation can be used to infer the yield that could be achieved with a more energetic driver if the same core conditions produced on OMEGA were realized on a larger system, referred to as hydrodynamic scaling[15–17]. Note that hydrodynamic scaling takes into account only the geometric benefits of driving a larger system. If α particle deposition is considered, any increase in α heating comes as the result of the hot-spot volume growing proportional to the laser energy E, not because of an increase in compression. When scaling up to the energy available at the NIF, this essentially amounts to multiplying the OMEGA χ by a factor $(E_{NIF}/E_{\Omega})^{1/3} \approx 4.2$.

Laser energy delivery with the multi-pulse driver

Short of major renovations to the laser itself, bumping the laser energy above the 28.5 kJ level that is consistently delivered on OMEGA requires greater conversion from the natural 1,053 nm (infra-red) line of an Nd:glass laser to the frequency-tripled (3ω) ultraviolet light that irradiates the target. This is done by ramping up near the 30 TW limit earlier in the drive and compressing the pulses in time (shortening them below 2 ns), and/or employing the multi-pulse driver technique, which turns off smoothing by spectral dispersion (SSD)[50] during the main drive. These improve frequency conversion efficiency and can make available up to 31.5 kJ of UV energy on target, around 10% higher than with full-bandwidth SSD on during the entire pulse. Turning off SSD also causes an effective shrinking of the beam diameter by around 10%, which reduces the CBET and enhances the absorption.

Experimental diagnostics

Several important measurements need to be made to properly infer the hot-spot internal energy. From equation (20), we see that measurements of the average ion and electron temperature, the hot-spot radius, the burnwidth and the neutron yield constitute the requisite parameters for this calculation. This is made possible by the Omega Laser Facility's comprehensive suite of diagnostics. The energy spectrum obtained by neutron time-of-flight detectors[30] are able to reveal not only the DT and DD neutron yields also but the ion temperature. Cu activation

detectors[24] are also used to measure the neutron yield. Areal densities are measured on the nTOF via neutrons backscattered off of plasma ions, and on a magnetic recoil spectrometer[51] using forward scattering. Images of the hot spot are taken by the single line-of-sight time-resolved X-ray imager[29], Kirkpatrick–Baez framing camera, gated monochromatic X-ray imaging diagnostic and spatially resolved electron temperature diagnostic[31]. The burnwidth (duration) and bang time (time of peak neutron rate) are measured by the neutron temporal diagnostic[28].

Data availability

Raw data were generated at the Laboratory for Laser Energetics and are not available to the general public. Derived data supporting the findings of this study are available from the corresponding authors upon request.

Code availability

The simulation codes used in this paper are not available to the general public.

References

49. Cao, D. et al. Interpreting the electron temperature inferred from x-ray continuum emission for direct-drive inertial confinement fusion implosions on OMEGA. *Phys. Plasmas* **26**, 082709 (2019).
50. Skupsky, S. et al. Improved laser beam uniformity using the angular dispersion of frequency modulated light. *J. Appl. Phys.* **66**, 3456–3462 (1989).
51. Gatu Johnson, M. Charged particle diagnostics for inertial confinement fusion and high-energy-density physics experiments. *Rev. Sci. Instrum.* **94**, 021104 (2023).

Acknowledgements

We thank P. Patel for discussions regarding the relationship between neutron and X-ray emission. This report was prepared as an account of work sponsored by an agency of the US Government. Neither the US Government nor any agency thereof, nor any of their employees, makes any warranty, express or implied, or assumes any legal liability or responsibility for the accuracy, completeness or usefulness of any information, apparatus, product or process disclosed, or represents that its use would not infringe privately owned rights. Reference herein to any specific commercial product, process or service by trade name, trademark, manufacturer or otherwise does not necessarily constitute or imply its endorsement, recommendation or favouring by the US Government or any agency thereof. The views and opinions of authors expressed herein do not necessarily state or reflect those of the US Government or any agency thereof. This work was performed at the Laboratory for Laser Energetics for the US Department of Energy National Nuclear Security Administration under grant no. DE-NA 0003856, and grants no. DE-SC0021072 and DE-SC0022132 from the Department of Energy Office of Fusion Energy Science. Funding for the targets utilized in this study was provided by General Atomics and funded through NNSA contract 89233119CNA000063.

Author contributions

C.A.W. and R.B. conceived the study and wrote the paper. V.G., R.B., A.L. and R.E. developed predictive models used to design high-performance experiments. V.G., C.A.W., R.B., J.P.K., A.L., D.C., P.S.F., R.Ejaz., C.A.T., W.T., M.J.R., S.P.R., C.Stoeckl. and V.N.G. designed and executed experiments used in training the predictive models used for this work. V.G., C.A.W., R.B., A.L. D.P., J.P.K. and C.J.F designed and executed the high-performance experiment series. D.C., K.S.A., R.Epstein., J.C.-N., I.V.I., J.A.M., P.B.R., T.J.B.C., S.X.H., W.S. and V.N.G. contributed to the radiation–hydrodynamic simulation development used in this work. V.G., C.J.F., V.Y.G., W.T., D.H.E., S.I., M.J.R., H.M.C., M.G.J., R.D.P., J.A.F., R.C.S. and S.P.R. contributed to the development and analysis of diagnostics used in this work. D.B, C.F., M.K., R.T.J., M.J.B., J.M., B.S., D.G., C.Shuldberg., M.F. and D.R.H. were responsible for fielding the implosion targets used in this work. K.A.B., S.S. and L.J.W. were responsible for managing the OMEGA laser. M.L. and S.F.B.M. were responsible for managing the Omega facility and experimental operations. E.M.C. and C.D. were responsible for project management for the Laboratory for Laser Energetics.

Competing interests

The authors declare no competing interests.

Additional information

Extended data is available for this paper at https://doi.org/10.1038/s41567-023-02363-2.

Correspondence and requests for materials should be addressed to C. A. Williams.

Peer review information *Nature Physics* thanks Vladimir Tikhonchuk and the other, anonymous, reviewers for their contribution to the peer review of this work.

Reprints and permissions information is available at www.nature.com/reprints.

https://doi.org/10.1038/s41567-023-02363-2

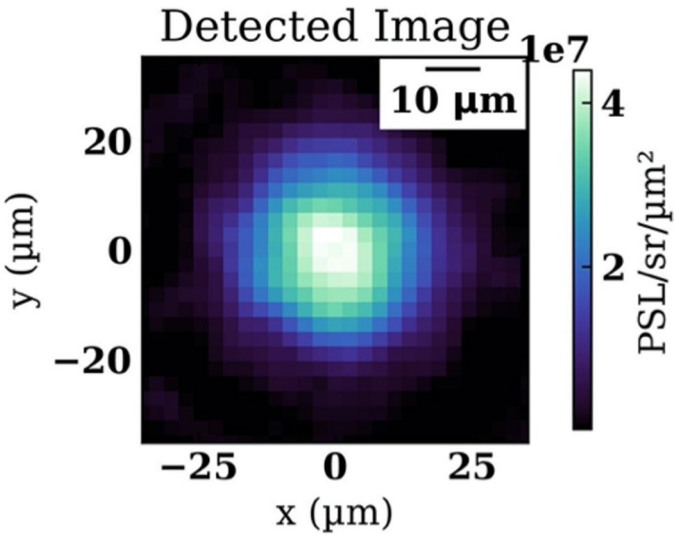

Extended Data Fig. 1 | SRTe x-ray Image. Spatially resolved electron temperature (SRTe) diagnostic experimental x-ray image of shot number 102154. The photon simulated luminescence (PSL) is an analog for brightness. Fourier analysis of the hot-spot modes show that the $\ell = 2$ mode is typically dominant in OMEGA implosions, and the inferred hot-spot volumes account for ellipticity. The majority of recent high-yield OMEGA implosions are round, with low semi-major to semi-minor axis ratios a/b. For example, shot 102154 has a/b = 1.03 ± 0.02.